Journal of Materials Chemistry A

PAPER

View Article Online
View Journal | View Issue

Cite this: J. Mater. Chem. A, 2018, 6, 8742

Boosting supercapacitive performance of ultrathin mesoporous $NiCo_2O_4$ nanosheet arrays by surface sulfation†

Yuxiu You,[a] Maojun Zheng, *[ab] Dongkai Jiang,[a] Fanggang Li,[a] Hao Yuan,[a] Zhihao Zhai,[a] Li Ma[c] and Wenzhong Shen[a]

Surface functionalization is as an effective way to modulate the electrochemical or photoelectrochemical properties of nanomaterials. Sulfated ultrathin mesoporous $NiCo_2O_4$ nanosheet arrays are fabricated based on a convenient galvanic displacement process, exhibiting stimulated chemical reactivity and boosted supercapacitive performance. This method not only realizes synchronization of synthesis and surface functionalization but also readily tailors the functionalizing degree of the sulfate-ion and surface reactivity of $NiCo_2O_4$ through adjusting the addition amount of the sulfur source. Moderately sulfated $NiCo_2O_4$ exhibits a capacitance activation in the first 2100 cycles and achieves the highest specific capacitance of up to 1113 F g^{-1}, an increase of 57% over that of pristine $NiCo_2O_4$ during 5000 cycling tests at a high current density of 5 A g^{-1}. Additionally, the sample displays an outstanding cycling performance with 166% capacitance retention. On the basis of structural characterization and surface chemical analysis, this research puts forward a scientific explanation for significantly boosting the electrochemical performance by surface sulfation. In addition, we present a facile route for fabricating sulfated metal oxides without post-processing for energy conversion and storage fields.

Received 10th February 2018
Accepted 11th April 2018

DOI: 10.1039/c8ta01442f

rsc.li/materials-a

1. Introduction

The increasing energy crisis associated with environmental pollution and global warming[1–3] compels humanity to search for clean and renewable power sources as well as efficient energy storage technologies.[4,5] In recent years, supercapacitors, one of the energy-storage devices, are of considerable interest by virtue of their long cycling life, fast charge–discharge process and pollution-free operation.[6–8] In comparison with various electrode materials including carbon,[9] polymers[10] and transition metal hydroxides,[11] mixed transition metal oxides (MTMO) coupled with different metal species possess unique features with high capacitance, electronic conductivity and rich redox reactions, playing promising roles in supercapacitors.[12–14] Among these MTMO materials, $NiCo_2O_4$ has been widely investigated due to its appealing characteristics of low cost, nontoxicity, natural abundance and superior supercapacitive performance.[12,15,16] To promote the electrochemical performance, most studies have been devoted to fabricating various nanostructures with a large surface area or good conductive composites, for instance Fe-doped $NiCo_2O_4$ microspheres@nanomeshes,[17] $NiCo_2O_4$ tetragonal microtubes,[18] $NiCo_2O_4$ hollow spheres,[13] $NiCo_2O_4$@Ni_3S_2 core/shell nanothorns[6] and TiN@$NiCo_2O_4$ coaxial nanowires.[19] Nevertheless, these strategies still do not lead to a satisfactory capacity because the insufficient surface reactivity is a hindrance to fully realize its storage capability. The charge storage mechanism of $NiCo_2O_4$ mainly based on redox reactions is closely related to the surface chemistry and electronic structure of the material. Surface functionalization can modulate the surface electronic structure and chemical environment and then boost the electrochemical performance of active materials.

Surface functionalization has been widely used for carbon electrode materials;[20–22] however, there are still very few reports on surface functionalization of transition metal oxides for supercapacitors.[23] Bai *et al.* reported NiO nanofibers functionalized with citric acid as a supercapacitor electrode which exhibited a much higher specific surface area and specific capacitance (336 F g^{-1}) than those of pristine NiO (136 F g^{-1}).[24] Recently, Xia and co-workers found that phosphate ion functionalized Co_3O_4 nanosheets could significantly increase the number of surface active sites and reduce charge transfer resistance, leading to greatly improved capacitive performance (up to approximately eightfold enhancement of specific capacitance).[23] Lu *et al.* synthesized phosphorylated TiO_2 nanotube arrays greatly

[a]Key Laboratory of Artificial Structure and Quantum Control, Ministry of Education, School of Physics and Astronomy, Shanghai Jiao Tong University, Shanghai, 200240, PR China. E-mail: mjzheng@sjtu.edu.cn; Fax: +86-021-54741040

[b]Collaborative Innovation Center of Advanced Microstructures, Nanjing University, Nanjing, 210093, PR China

[c]School of Chemistry and Chemical Technology, Shanghai Jiao Tong University, Shanghai, 200240, PR China

† Electronic supplementary information (ESI) available. See DOI: 10.1039/c8ta01442f

boosting sodium storage.[25] As one kind of efficient functionalization strategies, sulfation has been successfully used in various catalyst fields, effectively enhancing catalytic reactivity.[26–32] Gao *et al.* illustrated that sulfated oxides displayed high thermostability, very strong acidity and high catalytic reactivity.[26] Liu *et al.* synthesized sulfated porous Fe–Ti bimetallic solid superacid catalysts, which showed high reactivity for efficient photochemical oxidation of azo dyes under visible light.[28] As noted above, we anticipate that sulfation can endow ultrathin mesoporous $NiCo_2O_4$ nanosheet arrays with higher surface chemical reactivity. To the best of our knowledge, until now, sulfated $NiCo_2O_4$ applied in supercapacitors has not been reported.

In this work, we develop a facile galvanic displacement approach to synthesize sulfated ultrathin mesoporous $NiCo_2O_4$ nanosheet arrays. Moderately sulfated $NiCo_2O_4$ exhibits an increased capacitance far exceeding that of pristine $NiCo_2O_4$ (~57%) at a high current density of 5 A g^{-1} and a superior cycling stability with 166% capacity retention after testing for 5000 cycles. This remarkable supercapacitive performance can be ascribed to several merits. The unique ultrathin mesoporous nanosheet arrays provide a large surface area for faradaic reactions and short channels for ion diffusion and charge transfer. Sulfation improves the surface reactivity and electrode kinetics and introduces highly active sites, bringing about less energy requirement for faradaic reactions. Herein, we not only propose a facile route to effectively functionalize metal oxides for energy conversion and storage but also establish a basic comprehension of the correlation between sulfation and the capacitive enhancement of $NiCo_2O_4$.

2. Experimental section

2.1 Materials and methods

Nickel foam with an area of 1 cm × 4 cm pressed by a 2 MPa force was cleaned in order with acetone and 2 M HCl in an ultrasound bath for 15 min and rinsed with ethanol and DI water several times. The sulfated ion functionalized $NiCo_2O_4$ was synthesized in a galvanic cell system with two half-cells. The Ni foam immersed into a mixed solution of 5 mM $NiCl_2$, 10 mM $CoCl_2$ and 0.25 M or 0.5 M thiourea was externally connected to a certain amount of an Al sheet dipped into 0.25 M NaOH with a copper wire. In addition, a saturated KCl salt bridge was used to connect the two half-cells. The experiment was conducted at room temperature for 1 h. The grown sample was washed with DI water and ethanol several times and then dried in air at 60 °C for 12 h. The dried sample was then annealed at 250 °C for 2 h in air. Without the addition of thiourea, the pristine $NiCo_2O_4$ can be fabricated under the same experimental conditions. For simplification, the sample grown in 0.25 M and 0.5 M thiourea is denoted as S0.25M and S0.5M, respectively. The weight of all samples was measured before deposition and after annealing, and the mass of active materials was 0.5 mg cm^{-2}.

2.2 Structural characterization

Powder X-ray diffraction (XRD) was performed using a Rigaku Ultima IV X-ray diffractometer with a Cu Kα radiation source. X-ray photoelectron spectroscopy (AXIS ULTRA DLD, Kratos, Japan) was also carried out to analyze the surface chemical composition and valance states of the samples. The details of the structure and morphology were observed by field emission scanning electron microscopy (FESEM, Zeiss Ultra Plus) and transmission electron microscopy (TEM) (JEOL JEM-2100F with an acceleration voltage of 200 kV).

2.3 Electrochemical measurements

We researched the electrochemical properties of all samples on Ni foam as the working electrode in a three-electrode installation with a SCE reference electrode and a Pt plate counter electrode in 2 M KOH. The cyclic voltammetry (CV) and electrochemical impedance spectroscopy (EIS) tests were performed on a CHI760B electrochemical workstation. The galvanostatic charge–discharge (GCD) measurements were conducted on a LAND CT-2001A. The calculation equation of specific capacitance is as follows:

$$C = \frac{It}{m\Delta V} \quad (1)$$

where C (F g^{-1}) is the specific capacitance, I (mA) is the current density, t (s) is the discharge time, m (mg) is the quantity of active materials, and ΔV (V) is the voltage window.

3. Results and discussion

The ultrathin mesoporous $NiCo_2O_4$ nanosheet arrays were synthesized by a solution-based galvanic displacement method and then annealed at 250 °C for 2 h in air, as illustrated in Fig. 1a. The details of the preparation process can be found in the Experimental section. The component of the as-deposited samples is indexed to Co–Ni layered double hydroxides from the XRD spectra in Fig. S1.† The XRD spectra in Fig. 1b show that the peaks at 31.2°, 36.5°, 59.2°, and 65.1° of pristine and sulfated $NiCo_2O_4$, excluding two intense peaks originating from Ni foam, can be well indexed to the (220), (311), (511), and (440) crystal planes of the spinel $NiCo_2O_4$ cubic phase (JCPDS no. 20-0781), respectively. Compared with the pristine $NiCo_2O_4$, the functionalized $NiCo_2O_4$ without any impurity peaks and shifting peaks is proven to be of high purity.

X-Ray photoelectron spectroscopy (XPS) of each element and its fitting results are further shown in Fig. 2a–d. The Ni 2p and Co 2p spectra are both fitted with two spin–orbit doublets and shakeup satellites. The XPS spectra of Ni 2p display two fitting peaks at 854.1 eV and 871.5 eV, which indicate the presence of Ni^{2+}.[33] The spin–orbit peaks of Ni $2p_{3/2}$ at 855.7 eV and Ni $2p_{1/2}$ at 873.2 eV correspond to the Ni^{3+} cation, which is in majority in Ni atoms in the crystal lattice. In the Co 2p spectra, two peaks with binding energies of 779.6 eV and 794.6 eV belong to the Co^{3+} cation and the other peaks at 781.1 eV and 796.3 eV are indexed to the Co^{2+} cation.[34] The O 1s spectra show four different oxygen contributions, three peaks of which, at 529.5, 531.8 and 532.9 eV, are associated with the metal oxide, number of defect sites and water adsorbed on the surface, respectively.[35] The O 1s spectra of pristine and sulfated $NiCo_2O_4$ both have a peak at 531.00 eV, originating from OH^- and SO_4^{2-} groups, respectively.[36–38] The

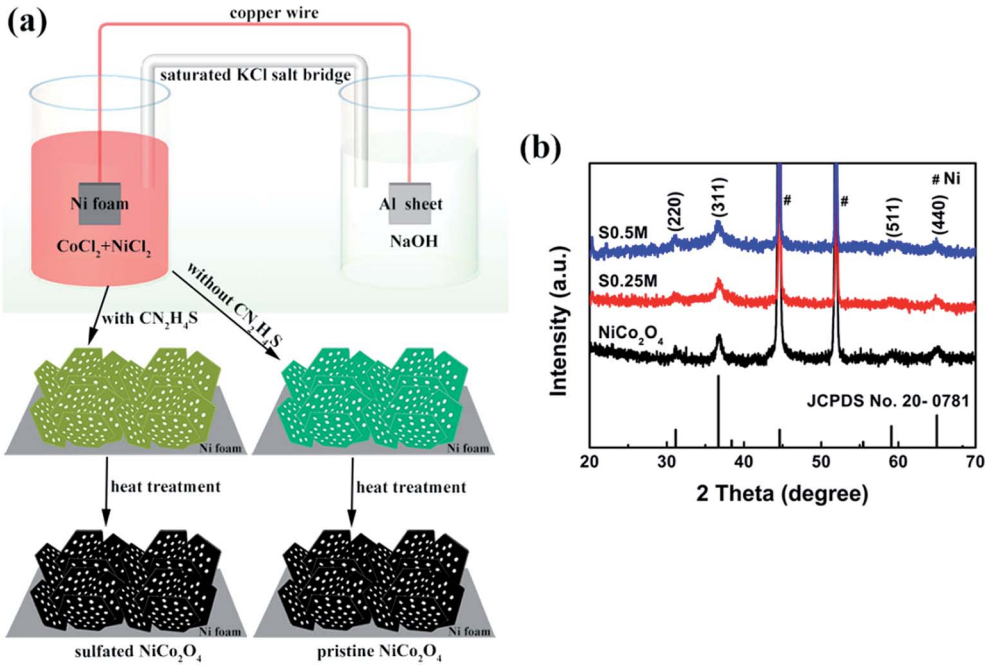

Fig. 1 (a) Schematic of synthesizing pristine and sulfated $NiCo_2O_4$ nanosheet arrays on Ni foam; (b) XRD spectra of synthesized sulfated $NiCo_2O_4$, S0.25M and S0.5M.

peak intensity at 531.0 eV improves with increasing sulfate content , implying that the OH^- group on the $NiCo_2O_4$ surface has been replaced by the SO_4^{2-} group during the surface sulfation process. The core-level S 2p spectra in Fig. 3d show a broader peak centered at 168.5 eV, which can be attributed to SO_4^{2-}.[27,28] Moreover, the peak intensity of SO_4^{2-} is proportional to the added thiourea concentration, which is consistent with Fig. 2c.

The field-emission scanning electron microscopy (FESEM) images of the as-prepared $NiCo_2O_4$ nanosheet arrays are given in Fig. 3. Fig. 3a–c present the pristine $NiCo_2O_4$, S0.25M and S0.5M with a similar porous array micro-structure formed by cross stacking of numerous independent mesoporous nanosheets. These independent nanosheets with clearly observed mesopores have a planar gauze-like morphology with several hundred

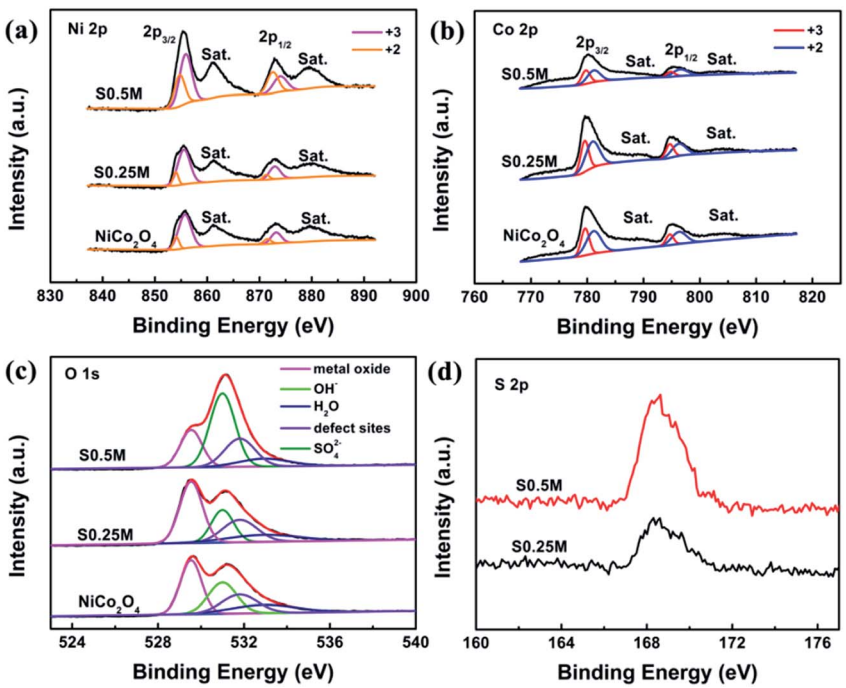

Fig. 2 The XPS spectra of $NiCo_2O_4$, S0.25M and S0.5M: (a) Ni 2p spectra, (b) Co 2p spectra, (c) O 1s spectra, (d) S 2p spectra.

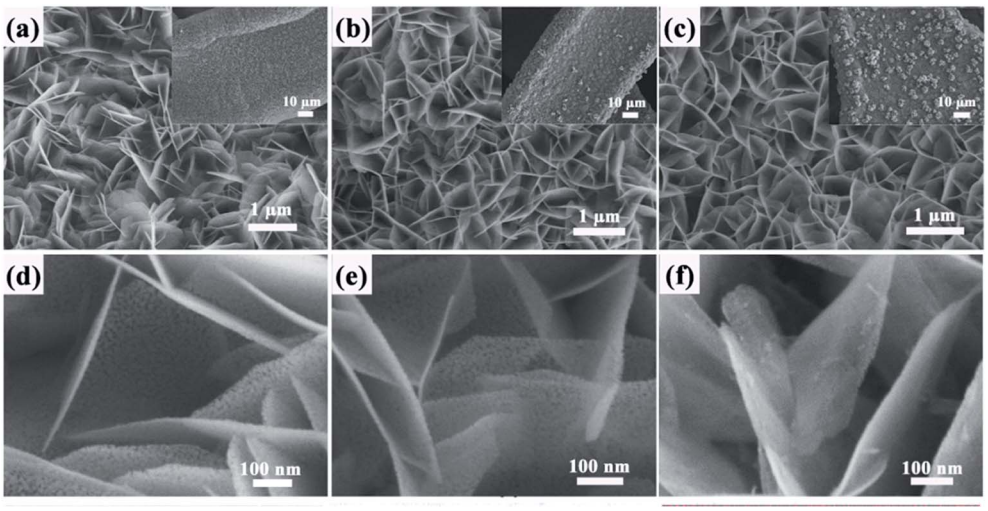

Fig. 3 The low- and high-magnified SEM images of (a and d) $NiCo_2O_4$, (b and e) S0.25M and (c and f) S0.5M. Insets in the upper-row figures show the different distributions of $NiCo_2O_4$, S0.25M and S0.5M nanosheets on Ni foam.

nanometers in lateral dimension. This open porous architecture can provide abundant surface reactive sites and enough ion storage space for fast faradaic reactions.[39] However, there are still some differences in morphology and distribution between the three different samples, the crook degree and the number of whose nanosheets is in proportion to the added amount of thiourea as shown in the insets. The introduction of thiourea to the precursor solution is beneficial to form the nanosheet.

The transmission electron microscopy (TEM) measurements were further employed to investigate the structure of the synthesized $NiCo_2O_4$ nanosheets. From Fig. 4, the nanosheets of pristine $NiCo_2O_4$ are composed of lots of nanoparticles with a size of about 12 nm consistent with the result calculated using the Scherrer equation (see the ESI†). The mesopores between these nanoparticles mainly range from 2 to 5 nm, resulting from thermal annealing of the precursor. Unlike pristine $NiCo_2O_4$, the nanoparticles in S0.25M have no obvious edge and tend to interconnect, suggesting that the surface is reconstructed due to the introduction of the sulfate ion. Besides, the well-defined diffraction rings displayed in the selected-area electron diffraction (SAED) patterns of $NiCo_2O_4$ and S0.25M both illustrate their polycrystalline nature. In accordance with the XRD results, these rings can be satisfactorily ascribed to the (220), (311), (400) and (440) crystal planes of the cubic $NiCo_2O_4$ phase, indicating that sulfation will not change the crystal structure.

The pristine and sulfated $NiCo_2O_4$ nanosheet arrays on Ni foam were used as binder-free electrodes for supercapacitors to evaluate their electrochemical properties. Fig. 5 shows the representative cyclic voltammogram (CV) curves at various sweep rates in the range from 5 to 100 mV s^{-1} in the potential window of 0–0.6 V *vs.* SCE. A pair of distinct redox peaks of the CV curves is derived from reversible faradaic reactions, clearly revealing the conventional faradaic behaviors of this battery-type electrode.[4,40] The reversible redox reactions in sulfated $NiCo_2O_4$ are inferred as the following equations:

$$NiCo_2O_{4-x}(SO_4^{2-})_x + OH^- + H_2O \leftrightarrow NiO_{1-y}(SO_4^{2-})_yOH + 2CoO_{1-(x-y)/2}(SO_4^{2-})_{(x-y)/2}OH + e^- \quad (2)$$

$$CoO_{1-(x-y)/2}(SO_4^{2-})_{(x-y)/2}OH + OH^- \leftrightarrow CoO_{2-(x-y)/2}(SO_4^{2-})_{(x-y)/2} + H_2O + e^- \quad (3)$$

Significantly, with the gradual increase of scan rates, the shape of these CV curves can be maintained well except a slight

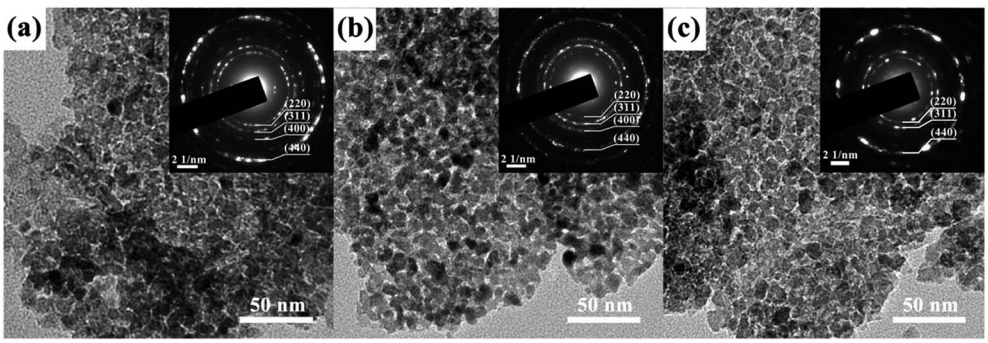

Fig. 4 The TEM images and the SAED pattern (insets) of (a) $NiCo_2O_4$, (b) S0.25M and (c) S0.5M.

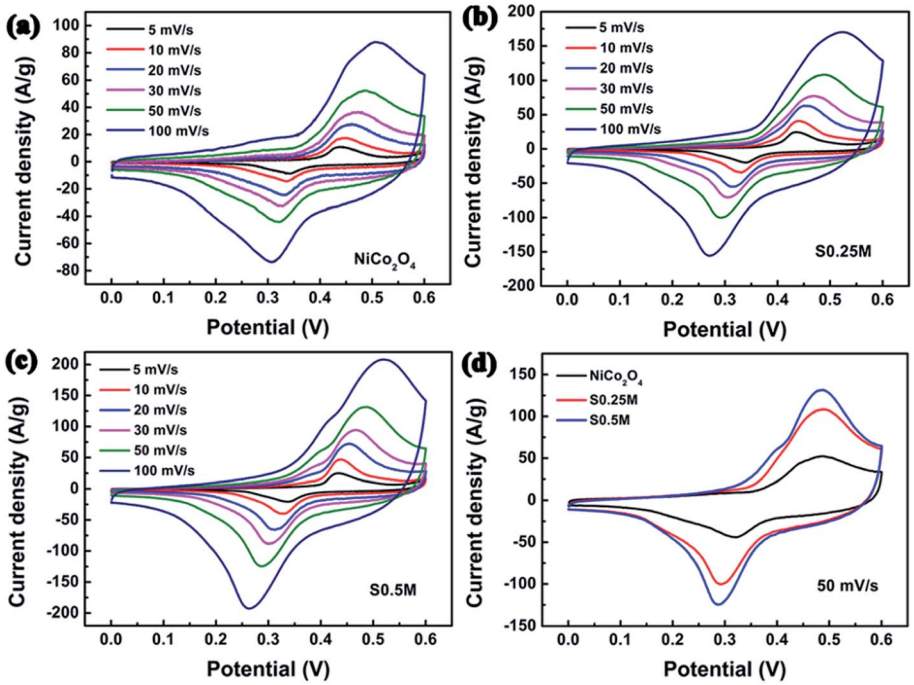

Fig. 5 CV curves of (a) $NiCo_2O_4$, (b) S0.25M and (c) S0.5M at scan rates ranging from 5 mV s^{-1} to 100 mV s^{-1}; (d) CV curves of $NiCo_2O_4$, S0.25M and S0.5M at 50 mV s^{-1}.

shift of the peak position, suggesting that the fast redox reactions occur in the electrode. As can be seen from Fig. 5d, the area relationship of CV curves at a scan rate of 50 mV s^{-1} between pristine and sulfated $NiCo_2O_4$ is $A_{S0.5M} > A_{S0.25M} > A_{\text{pristine } NiCo_2O_4}$.

The galvanostatic charge–discharge measurements were carried out with the potential window between 0 and 0.53 V (*vs.* SCE) to investigate the specific capacitances of the electrodes. Consistent with the CV measurements, pronounced voltage plateaus corresponding to the redox couple can be observed from the galvanostatic charge–discharge curve profiles as shown in Fig. 6a. Furthermore, the symmetric shapes of these curves imply good reversibility of redox reactions.[41] The specific capacitance as a function of current density for pristine and sulfated ion functionalized $NiCo_2O_4$ is plotted in Fig. 6b. Remarkably, $NiCo_2O_4$, S0.25M and S0.5M deliver specific capacitances of 390.56, 524.52, and 656.6 F g^{-1} at a current density of 1 A g^{-1}, respectively. Surprisingly, the specific capacitance increases rapidly as the current density increases, which can be attributed to the capacitance activation. When the current density increases from 1 to 40 A g^{-1}, the specific capacitance retention is calculated to be 116, 144 and 138% for $NiCo_2O_4$, S0.25M and S0.5M, respectively.

The cycling stability of $NiCo_2O_4$, S0.25M and S0.5M was shown in Fig. 6c. All the samples exhibit capacitance activation in the first 1000 cycles. Due to the porous array architecture, with the gradual penetration of electrolyte into the interior structure, the inner active material is activated and participates in redox reactions, increasing the capacitance gradually.[42–44] After 1000 cycles, the specific capacitance of S0.5M decreases rapidly while the S0.25M presents the highest specific capacitance of 1113 F g^{-1} until the 2100th cycle, which is 1.57 times higher than that of pristine $NiCo_2O_4$ with the highest capacitance of 707 F g^{-1}. Moreover, the $NiCo_2O_4$, S0.25M and S0.5M, respectively, show a capacitance retention of 169, 166 and 112% after 5000 cycles. Accordingly, moderate sulfation can greatly improve the capacitive performance for $NiCo_2O_4$.

In order to investigate the influence of long-term cycling tests on the morphology and structure, SEM and TEM measurements are further conducted for all samples after 5000 cycles. From Fig. S2 and S3,† it can be seen that all samples maintain a good porous-array structure and ultrathin morphology except for some slightly collapsed nanosheets, implying the negligible influence of activation and charge–discharge cycle process on the structure and morphology. The S 2p core-level XPS spectra of the sulfated samples after being fully activated are further measured to investigate the reason for the capacitance decrease of S0.5M (see Fig. S4†). After being fully activated, S0.5M loses almost all sulfate ions while S0.25M retains the majority of its sulfate ions, indicating that excess sulfate ion functionalization gives rise to the unstable surface chemistry or electronic structure which results in easy and rapid loss of sulfate ions. Thus, a higher level of sulfation causes more capacitance decrease after the activation process.

To further research the resistive capacity of the active materials, electrochemical impedance spectroscopy was performed at an open circuit potential in the frequency range of 0.1–100 kHz. From the Nyquist plots of the different samples in Fig. 6d, the equivalent series resistances of $NiCo_2O_4$, S0.25 and S0.5M were 0.58, 0.6 and 0.55 Ω, respectively, implying the low internal resistance of the electrode and good adhesion to the substrate of the active materials.[45] Compared with pristine

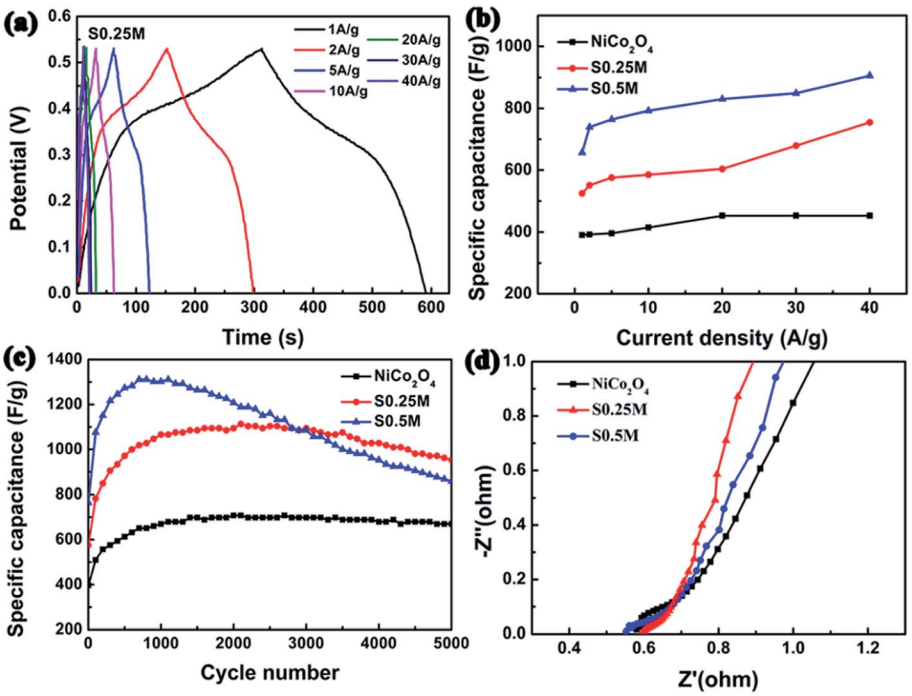

Fig. 6 (a) The galvanostatic charge–discharge curves at various current densities of S0.25M; (b) the specific capacitances at different current densities, (c) cycling performance at a current density of 5 A g^{-1} and (d) Nyquist plots of $NiCo_2O_4$, S0.25M and S0.5M

$NiCo_2O_4$, S0.25M and S0.5M exhibited smaller semicircles and more vertical lines, indicating the enhancement in charge transfer and ion diffusion.[1,46] In comparison with S0.25M, S0.5M shows a smaller slope and a larger semicircle, which indicate that excess sulfate ions prevent the decrease of electron transmission and ion diffusion resistance and facilitate fast redox reactions.

To comprehend the correlation between surface sulfation and enhanced electrochemical performance, we further research the surface electronic structure and chemical reactivity. The introduction of sulfate ions changes the chemical bonds and corresponding electronic chemical environment of metal sites, thus significantly promoting surface reactivity.[23] The length of the Co–O bond of about 1.855 Å is shorter than that of Co–SO_4, which is about 2.0 Å. Furthermore, the Pauling electronegativity of –SO_4 is calculated to be 3.225,[47] smaller than that of the O element (3.44). The covalent character of the Co–SO_4 bond is further estimated to be 63.6%, higher than that of the Co–O bond which is about 54.4%. The sulfate functionalized $NiCo_2O_4$ with a longer bond and higher covalent character needs less energy for

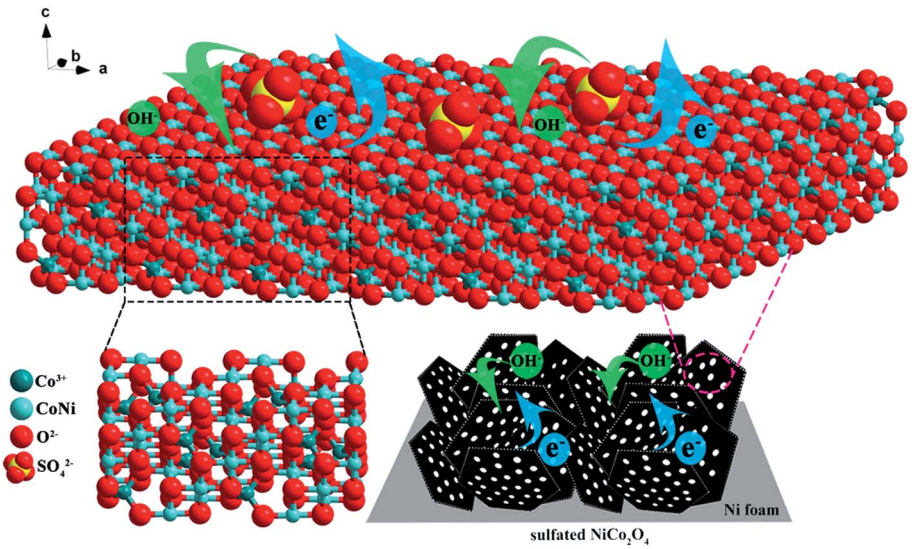

Fig. 7 Schematic of the functionalized surface and redox reaction process in the sulfated $NiCo_2O_4$ nanosheet arrays.

redox reactions to occur than that required before functionalization, thus enhancing surface reactivity and electrode kinetics. Fig. 7 gives the schematic illustration of the functionalized surface, redox reaction process and electronic structure of the functionalized $NiCo_2O_4$. The ultrathin mesoporous morphology and open porous arrays provide a large surface area with lots of active sites and "ion reservoir" providing enough electrolyte ions for fast redox reactions at high current densities. The synergistic effect of structure and moderate sulfation facilitates electron transmission and improves surface reactivity, thus resulting in high capacity and excellent stability.

4. Conclusion

In summary, we fabricate sulfated ultrathin mesoporous $NiCo_2O_4$ nanosheet arrays on Ni foam using a facile self-assembly technique without conventional post-processing. Adjusting the addition amount of the sulfur source can readily tailor the functionalized degree of the sulfate-ion and surface reactivity of $NiCo_2O_4$. The surface reactivity of the $NiCo_2O_4$ nanosheet arrays is boosted by surface sulfation. Benefiting from the enhanced surface activity, electrode kinetics and unique nanosheet array structure, the moderately functionalized $NiCo_2O_4$ (S0.25M) achieves a fascinating electrochemical performance with excellent stability and much higher capacitance far exceeding that of the pristine sample at a high current density of 5 A g^{-1}. Given the excellent electrochemical performance and facile synthesis process, we believe this sulfation strategy is a promising route to fabricate enhanced-performance electrodes for energy conversion and storage.

Conflicts of interest

There are no conflicts to declare.

Acknowledgements

The authors gratefully thank the support of this work by the National Natural Science Foundation of China (grant no. 11174197 and 11574203) and the support for SEM tests from the Center for Advanced Electronic Materials and Devices (AEMD) of Shanghai Jiao Tong University.

References

1 Y. X. Zhao, C. Chang, F. Teng, Y. F. Zhao, G. B. Chen, R. Shi, G. I. N. Waterhouse, W. F. Huang and T. R. Zhang, *Adv. Energy Mater.*, 2017, 1700005.
2 J. Liu, C. H. Liang, G. P. Xu, Z. F. Tian, G. S. Shao and L. D. Zhang, *Nano Energy*, 2013, **2**, 328–336.
3 A. González, E. Goikolea, J. A. Barrena and R. Mysyk, *Renewable Sustainable Energy Rev.*, 2016, **58**, 1189–1206.
4 Y. G. Wang, Y. F. Song and Y. Y. Xia, *Chem. Soc. Rev.*, 2016, **45**, 5925–5950.
5 G. P. Wang, L. Zhang and J. J. Zhang, *Chem. Soc. Rev.*, 2012, **41**, 797–828.
6 J. P. Wang, S. L. Wang, Z. C. Huang and Y. M. Yu, *J. Mater. Chem. A*, 2014, **2**, 17595–17601.
7 Z. S. Wu, X. L. Feng and H. M. Cheng, *Natl. Sci. Rev.*, 2013, **1**, 277–292.
8 X. Y. Liu, Y. Q. Gao and G. W. Yang, *Nanoscale*, 2016, **8**, 4227–4235.
9 M. S. Kim, E. Lim, S. Kim, C. Jo, J. Y. Chun and J. Lee, *Adv. Funct. Mater.*, 2016, **27**, 1603921.
10 J. X. Feng, L. X. Ding, S. H. Ye, X. J. He, H. Xu, Y. X. Tong and G. R. Li, *Adv. Mater.*, 2015, **27**, 7051–7057.
11 T. Yoon and K. S. Kim, *Adv. Funct. Mater.*, 2016, **26**, 7370.
12 D. P. Dubal, P. Gomez-Romero, B. R. Sankapal and R. Holze, *Nano Energy*, 2015, **11**, 377–399.
13 L. F. Shen, L. Yu, X. Y. Yu, X. G. Zhang and X. W. Lou, *Angew. Chem., Int. Ed.*, 2015, **54**, 1868–1872.
14 S. Gao, Y. F. Sun, F. C. Lei, L. Liang, J. W. Liu, W. T. Bi, B. C. Pan and Y. Xie, *Angew. Chem., Int. Ed.*, 2014, **53**, 12789–12793.
15 L. Qian, L. Gu, L. Yang, H. Yuan and D. Xiao, *Nanoscale*, 2013, **5**, 7388–7396.
16 G. Q. Zhang and X. W. Lou, *Adv. Mater.*, 2013, **25**, 976–979.
17 L. Liu, H. J. Zhang, L. Fang, Y. P. Mu and Y. Wang, *J. Power Sources*, 2016, **327**, 135–144.
18 F. X. Ma, L. Yu, C. Y. Xu and X. W. Lou, *Energy Environ. Sci.*, 2016, **9**, 862–866.
19 M. Y. Liu, T. Yang, J. H. Chen, L. Su, K. C. Chou and X. M. Hou, *J. Alloys Compd.*, 2017, **692**, 605–613.
20 A. T. Chidembo, K. I. Ozoemena, B. O. Agboola, V. Gupta, G. G. Wildgoose and R. G. Compton, *Energy Environ. Sci.*, 2010, **3**, 228–236.
21 H. Yoo, M. Min, S. Bak, Y. Yoon and H. Lee, *J. Mater. Chem. A*, 2014, **2**, 6663–6668.
22 N. Xiao, D. Lau, W. H. Shi, J. X. Zhu, X. C. Dong, H. H. Hng and Q. Y. Yan, *Carbon*, 2013, **57**, 184–190.
23 T. Zhai, L. M. Wan, S. Sun, Q. Chen, J. Sun, Q. Y. Xia and H. Xia, *Adv. Mater.*, 2016, **29**, 1604167.
24 B. Ren, M. Q. Fan, Q. Liu, J. Wang, D. L. Song and X. F. Bai, *Electrochim. Acta*, 2013, **92**, 197–204.
25 J. Ni, S. Fu, Y. Yuan, L. Ma, Y. Jiang, L. Li and J. Lu, *Adv. Mater.*, 2018, 1704337.
26 W. M. Hua, Y. D. Xia, Y. H. Yue and Z. Gao, *J. Catal.*, 2000, **196**, 104–114.
27 Z. H. Xu, C. Huang, L. Wang, X. X. Pan, L. Qin, X. W. Guo and G. L. Zhang, *Ind. Eng. Chem. Res.*, 2015, **54**, 4593–4602.
28 L. Qin, G. L. Zhang, Z. Fan, Y. J. Wu, X. W. Guo and M. Liu, *Chem. Eng. J.*, 2014, **244**, 296–306.
29 X. Wang, W. S. Liu, X. Lu and P. S. Lee, *J. Mater. Chem.*, 2012, **22**, 23114–23119.
30 P. Mohapatra, J. Moma, K. M. Parida, W. A. Jordaan and M. S. Scurrell, *Chem. Commun.*, 2007, 1044–1046.
31 S. Selvam, B. Balamuralitharan, S. N. Karthick, A. D. Savariraj, K. V. Hemalatha, S.-K. Kim and H.-J. Kim, *J. Mater. Chem. A*, 2015, **3**, 10225–10232.
32 Z. Zhang, J. Huang, H. Xia, Q. Dai, Y. Gu, Y. Lao and X. Wang, *J. Catal.*, 2018, **360**, 277–289.
33 R. Chen, H. Y. Wang, J. W. Miao, H. B. Yang and B. Liu, *Nano Energy*, 2015, **11**, 333–340.

34 X. H. Gao, H. X. Zhang, Q. G. Li, X. G. Yu, Z. L. Hong, X. W. Zhang, C. D. Liang and Z. Lin, *Angew. Chem., Int. Ed.*, 2016, **55**, 6290–6294.
35 C. Z. Yuan, J. Y. Li, L. R. Hou, X. G. Zhang, L. F. Shen and X. W. Lou, *Adv. Funct. Mater.*, 2012, **22**, 4592–4597.
36 H. Cheng, Y.-Z. Su, P.-Y. Kuang, G.-F. Chen and Z.-Q. Liu, *J. Mater. Chem. A*, 2015, **3**, 19314–19321.
37 J. S. Wei, H. Ding, P. Zhang, Y. F. Song, J. Chen, Y. G. Wang and H. M. Xiong, *Small*, 2016, **12**, 5927–5934.
38 C. D. Wagner, D. A. Zatko and R. H. Raymond, *Anal. Chem.*, 1980, **52**, 1445–1451.
39 C. Z. Yuan, L. Yang, L. R. Hou, L. F. Shen, X. G. Zhang and X. W. Lou, *Energy Environ. Sci.*, 2012, **5**, 7883–7887.
40 M. Salanne, B. Rotenberg, K. Naoi, K. Kaneko, P. L. Taberna, C. P. Grey, B. Dunn and P. Simon, *Nat. Energy*, 2016, **1**, 16070.
41 Y. X. You, M. J. Zheng, L. G. Ma, X. L. Yuan, B. Zhang, Q. Li, F. Z. Wang, J. N. Song, D. K. Jiang, P. J. Liu, L. Ma and W. Z. Shen, *Nanotechnology*, 2017, **28**, 105604.
42 D. S. Sun, Y. H. Li, Z. Y. Wang, X. P. Cheng, S. Jaffer and Y. F. Zhang, *J. Mater. Chem. A*, 2016, **4**, 5198–5204.
43 Y. G. Zhu, Y. Wang, Y. Shi, Z. X. Huang, L. Fu and H. Y. Yang, *Adv. Energy Mater.*, 2014, **4**, 1301788.
44 Y. Q. Zhang, X. H. Xia, J. P. Tu, Y. J. Mai, S. J. Shi, X. L. Wang and C. D. Gu, *J. Power Sources*, 2012, **199**, 413–417.
45 X. H. Xiong, D. Ding, D. C. Chen, G. Waller, Y. F. Bu, Z. X. Wang and M. L. Liu, *Nano Energy*, 2015, **11**, 154–161.
46 S. X. Wu, K. S. Hui, K. N. Hui and K. H. Kim, *J. Mater. Chem. A*, 2016, **4**, 9113–9123.
47 S. G. Bratsch, *J. Chem. Educ.*, 1985, **62**, 101–103.